



CHORUS

This is the accepted manuscript made available via CHORUS. The article has been published as:

Quantum oscillations in $\text{Cu}_{\{x\}}\text{Bi}_{\{2\}}\text{Se}_{\{3\}}$ in high magnetic fields

B. J. Lawson, G. Li, F. Yu, T. Asaba, C. Tinsman, T. Gao, W. Wang, Y. S. Hor, and Lu Li
Phys. Rev. B **90**, 195141 — Published 21 November 2014

DOI: [10.1103/PhysRevB.90.195141](https://doi.org/10.1103/PhysRevB.90.195141)

Quantum Oscillations in $\text{Cu}_x\text{Bi}_2\text{Se}_3$ in High Magnetic Fields

B. J. Lawson¹, G. Li¹, F. Yu¹, T. Asaba¹, C. Tinsman¹, T. Gao¹, W. Wang¹, Y. S. Hor², and Lu Li¹

¹*Department of Physics, University of Michigan, Ann Arbor, MI 48109, USA*

²*Department of Physics, Missouri University of Science and Technology, Rolla, Missouri 65409, USA*

(Dated: October 22, 2014)

$\text{Cu}_x\text{Bi}_2\text{Se}_3$ has drawn much attention as the leading candidate to be the first topological superconductor and the realization of coveted Majorana particles in a condensed matter system. However, there has been increasing controversy about the nature of its superconducting phase. This study sheds light on ambiguity in the normal-state electronic state by providing a complete look at the quantum oscillations in magnetization in $\text{Cu}_x\text{Bi}_2\text{Se}_3$ at high magnetic fields up to 31 T. Our study focuses on the angular dependence of the quantum oscillation pattern in a low carrier concentration. As the magnetic field tilts from the crystalline c -axis to the ab -plane, the change of the oscillation period follows the prediction of the ellipsoidal Fermi surface. As the doping level changes, the 3D Fermi surface becomes quasi-cylindrical at high carrier density. Such a transition is potentially a Lifshitz transition of the electronic state in $\text{Cu}_x\text{Bi}_2\text{Se}_3$.

PACS numbers: 71.18.+y, 74.25.Ha, 74.25.Jb

I. INTRODUCTION

Topological superconductors are a novel phase of matter that have been theoretically predicted but yet to be experimentally verified. Among topological materials, topological superconductors are especially interesting because they are a platform to realize Majorana particles - an elusive particle that is its own antiparticle. Furthermore, topological superconductors have been proposed as a platform for topological quantum computation.¹⁻³ The robustness of the topological surface states makes this avenue an attractive alternative to traditional methods for realizing quantum computation.⁴

A topological superconductor must have a full superconducting gap in the bulk with odd parity pairing, and the Fermi surface must enclose an odd number of time reversal invariant momenta in the Brillouin zone, i.e. the Fermi surface must contain an odd number of high symmetry points such as Γ , Z , X , etc. It also has a topologically protected gapless surface state with Majorana fermions.¹ $\text{Cu}_x\text{Bi}_2\text{Se}_3$ has been proposed as a leading candidate for topological superconductivity⁵ and has sparked a lot of interest. Experiments have shown that by intercalating Cu between Se layers in the known topological insulator Bi_2Se_3 the compound becomes superconducting at 3.8 K.⁶

$\text{Cu}_x\text{Bi}_2\text{Se}_3$ has been confirmed to be a bulk superconductor with a full pairing gap by specific heat measurement.⁷ There are some reports of surface Andreev bound states through the observation of a Zero Bias Conductance Peak (ZBCP)⁸, but other reports suggest that the ZBCP can be removed with gating.⁹ The ZBCP was also not observed in recent works using scanning tunneling spectroscopy.¹⁰ ARPES measurements have argued against the topological superconducting mechanism in $\text{Cu}_x\text{Bi}_2\text{Se}_3$ by reporting an even number of time reversal invariant momenta in the Brillouin zone.¹¹ Both ARPES and quantum oscillation experiments show a Dirac dispersion in $\text{Cu}_x\text{Bi}_2\text{Se}_3$ - a characteristic feature of topo-

logical systems.^{12,13} The continued interest in $\text{Cu}_x\text{Bi}_2\text{Se}_3$ and the increasing controversy over its exotic phase calls for a more complete look at quantum oscillations in magnetization. This work is an expansion of our previous study of the de Haas-van Alphen effect in $\text{Cu}_{0.25}\text{Bi}_2\text{Se}_3$ ¹³ and now includes several samples at a variety of doping levels and complete angular dependence.

Mapping of the Fermi Surface reveals a closed ellipsoidal Fermi Surface that becomes increasingly elongated with increased carrier density. At high carrier concentration, the Fermi Surface crosses the Brillouin Zone boundary and becomes open and quasi-cylindrical. Also, amplitude damping analysis reveals a strongly anisotropic effective mass. In this report, we will first discuss how we use torque magnetometry to observe quantum oscillations. Second we will discuss the angular dependence of the oscillation frequencies. And third, we will cover the various damping mechanisms of the quantum oscillation amplitude and the parameters extracted from that analysis.

II. EXPERIMENT

Single crystals of $\text{Cu}_x\text{Bi}_2\text{Se}_3$ were grown by melting stoichiometric mixtures of high purity elements Bi (99.999%), Cu (99.99%), and Se (99.999%) in a sealed evacuated quartz tube then slowly cooling the mixture from 850°C down to 620°C at which point the crystal was quenched in cold water. The doping level was determined by the mole ratio of the reactants used in the crystal growth, but the nominal doping did not end up corresponding with the measured carrier concentration. Since we were unable to directly measure the Cu concentration, we look at how parameters evolve with increased carrier concentration rather than the unreliable nominal doping. The samples used in the study were cut out from larger boules. They are generally black, and the typical size is about 5 mm \times 2 mm \times 0.5 mm.

Quantum oscillations are used to resolve Fermi Surface geometry and to discover the electronic properties of topological materials. Oscillations in magnetization, the de Haas-van Alphen effect (dHvA effect), arise from the quantization of the Fermi Surface into Landau Levels.

To measure quantum oscillations in magnetization, M , we employed a highly sensitive torque magnetometry method. Torque magnetometry measures the anisotropy in the magnetic susceptibility of the sample by putting the sample in a tilted magnetic field, H , where both H and M are confined to the x-z plane. The torque is then given by $\vec{\tau} = \vec{M} \times \vec{H} = (M_z H_x - M_x H_z)\vec{j}$ and $|\vec{\tau}| = \chi_z H_z H_x - \chi_x H_x H_z = \Delta\chi H^2 \sin\phi \cos\phi$, where ϕ is the tilt angle of the magnetic field \vec{H} away from the crystalline \hat{c} axis and $\Delta\chi = \chi_z - \chi_x$.

We glue the sample to the head of a thin film cantilever. To provide a balance between strength for heavier samples and sensitivity, both brass cantilevers and Kapton cantilevers with a metalized surface were used. The brass cantilevers are thinner, 0.001 inch, but have a higher Young's modulus. Whereas the Kapton thin films are 0.003 inch thick, but have a lower Young's modulus. The magnetic torque was tracked by measuring the capacitance between the metal surface of the cantilever and a thin gold film underneath. An example of oscillations in the torque data after background subtraction is shown in Fig. 1 with a schematic of the experimental setup in the upper right corner. Oscillations arise from Landau Level quantization. The frequency of this oscillation is proportional to the cross section of the Fermi Surface, A , by the Onsager relation:

$$F_s = \frac{\hbar}{2\pi e} A. \quad (1)$$

To further analyze the oscillation pattern in the torque, a polynomial background is subtracted from the $\tau - H$ curve to get the oscillatory torque τ_{osc} . A Fast Fourier Transform (FFT) of the oscillatory τ_{osc} vs. $1/\mu_0 H$ is given in the lower left inset of Fig. 1 revealing a single Fermi pocket.

III. RESULTS

The dHvA effect was observed in all of our $\text{Cu}_x\text{Bi}_2\text{Se}_3$ crystals. A typical example of our data showing torque as a function of $1/\mu_0 H$ with the polynomial background subtracted is shown in Fig. 1. A single frequency of oscillations in magnetization reveals a single Fermi pocket. At 300 mK the oscillation frequency was measured as a function of angle up to 90° . We further measured the temperature dependence of the oscillation amplitude up to 25 K at two different angles. A detailed analysis of the temperature and angular dependence of the quantum oscillations revealed the following features: 1) a closed ellipsoidal Fermi Surface in the low carrier concentration samples by resolving quantum oscillations up to 90° , 2)

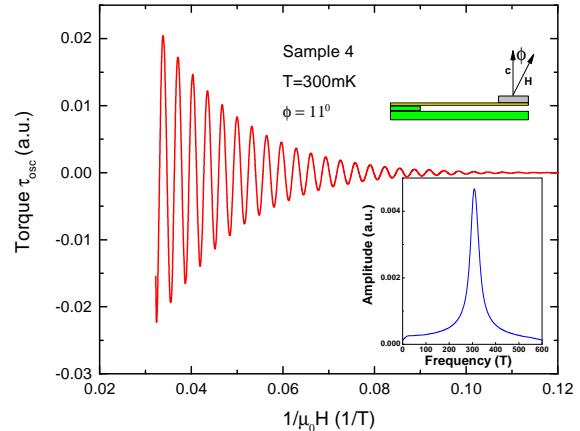


FIG. 1: (color online) Oscillations in the torque data of Sample 4 with a polynomial background subtracted. The inset in the upper right hand corner is a schematic of the experimental setup. The lower inset is a Fast Fourier Transformation (FFT) of the oscillatory torque after subtracting the polynomial background. The single peak in the FFT spectrum reveals a single Fermi pocket.

the Fermi surface gets progressively elongated in the z-direction as carrier concentration increases and becomes open at high carrier density, and 3) a strong anisotropy in the effective mass.

Figure 2 shows the torque signal from Sample 4. In Fig.2(a), oscillations are clearly seen up to 90° in the raw data indicating a closed Fermi surface. Fig.2(b) shows the FFT of the raw signal from panel a. Clear angular dependence can be tracked up to 90° , where H is parallel to the plane. Previous studies¹³ of the dHvA effect measured quantum oscillations up to 35° . The observation of quantum oscillations up to 90° is important confirmation of the previous result that the Fermi Surface is an ellipsoid.¹³ We note that the sample with this 3D Fermi surface is superconducting, and the Meissner effect of Sample 4 is shown in Fig. 7 and discussed in detail there.

Figure 3 shows the angular dependence of the oscillation frequency for the various samples. The dashed lines are ellipsoidal fits given by $F(\phi) = F_0(\cos^2[\phi] + (\frac{k_F^x}{k_F^z})^2 \sin^2[\phi])^{-\frac{1}{2}}$ where $F(\phi)$ is the frequency of the quantum oscillations at a particular ϕ , and the fitted parameters are F_0 (the quantum oscillation frequency at $\phi = 0^\circ$) and $\frac{k_F^x}{k_F^z}$ (a measure of the eccentricity of the Fermi surface). Most of the angular dependence of the oscillation frequencies are well fit by a closed, ellipsoidal Fermi Surface model; however, for the highest carrier concentration sample, a closed Fermi Surface fitting yields $k_F^z = 4.69 \text{ nm}^{-1}$, which is longer than the Brillouin Zone height¹⁴ of 3.28 nm^{-1} . Thus, it is clear that the Fermi Surface becomes open at high carrier concentration - which was

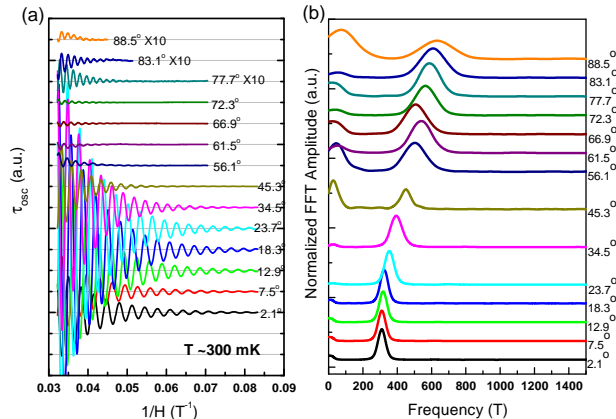


FIG. 2: (color online) (Panel a). Quantum oscillations in torque of Sample 4 at different angles after background subtraction. Oscillations are visible in the raw signal up to 90° . At high tilt angle, the oscillation signal is multiplied by a factor of 10 for clarity. (Panel b). The FFT spectra of oscillations in panel a show a single Fermi pocket with clear angular dependence. The FFT amplitude is normalized by the height of the peak in the range of 200 T - 600 T. For the high tilt angles, the divergence of FFT amplitude in the DC end arises from an incomplete background subtraction.

not seen in previous dHvA studies where there was only one sample of lower doping.¹³

The angular dependence of the quantum oscillation frequency provides the size of the Fermi pocket. From the Onsager relation, the frequency of the quantum oscillation is proportional to the cross-sectional area of the Fermi Surface given by $A = \pi k_F^x k_F^y(\phi)$, where $k_F(\phi)$ and k_F^x are the semi-major and semi-minor axes respectively of the elliptical Fermi surface cross-section. Thus F_0 yields $k_F^x = k_F^y$ and the eccentricity gives k_F^z . For Sample 4a, $k_F^x = k_F^y = 0.95 \text{ nm}^{-1}$ and $\frac{k_F^z}{k_F^x} = 2.06$. For a closed Fermi pocket, the bulk carrier concentration, n , is given by $n = \frac{1}{3\pi^2} k_F^x k_F^y k_F^z$. For sample 5, which has an open Fermi Surface, we calculated the bulk carrier concentration by integrating the ellipsoidal fit up to the Brillouin Zone boundary to find the volume of the Fermi surface. We assume that the deviation from the ellipsoidal fit around the Brillouin Zone boundary due to bending is small. In this case the carrier concentration is given by $n = \frac{1}{2\pi^2} k_F^x k_F^y (k_{BZ} - \frac{k_{BZ}^3}{k_F^z})$ where k_{BZ} is the $\Gamma - Z$ distance. This yields a carrier density n for Sample 5. The inferred carrier densities n are listed with other electronic parameters in Table I.

The value of k_F^z/k_F^x goes from 2.06 to 3.10 as the carrier concentration increases from $5.9 \times 10^{19} \text{ cm}^{-3}$ to $10.1 \times 10^{19} \text{ cm}^{-3}$ revealing that the Fermi Surface gets increasingly elongated in the z-direction as carriers are added. Then the Fermi Surface opens up and becomes quasi-cylindrical at high carrier concentration consistent with quantum oscillation measurements in magnetore-

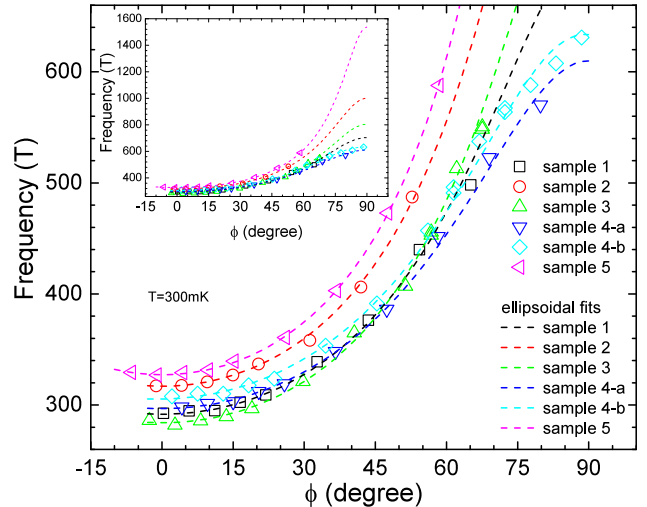


FIG. 3: (color online) Angular dependence of the oscillation frequency of the various samples. Dashed lines are ellipsoidal fits for the Fermi surfaces. The insert expands the y-axis of the data plot to a higher frequency range to show the extrapolation of the ellipsoidal fits.

TABLE I: Summary of results in order of increasing carrier concentration. *The value of k_F^z/k_F^x for sample 5 is ill-defined since k_F^z is taller than the Brillouin Zone. This is the value extracted from the ellipsoidal fit.

	$n(10^{19} \text{ cm}^{-3})$	$F_0(T)$	$k_F^x(\text{nm}^{-1})$	k_F^z/k_F^x
4a	5.93 ± 0.24	297 ± 1	0.95 ± 0.01	2.06 ± 0.05
4b	6.31 ± 0.20	306 ± 1	0.96 ± 0.01	2.09 ± 0.02
1	6.78 ± 0.73	292 ± 1	0.94 ± 0.01	2.41 ± 0.25
3	7.65 ± 0.35	284 ± 1	0.93 ± 0.01	2.83 ± 0.09
2	10.05 ± 1.18	317 ± 1	0.98 ± 0.01	3.16 ± 0.36
5	13.91 ± 2.71	327 ± 1	1.00 ± 0.01	$(4.69 \pm 0.79)^*$

sistence.¹¹

The effective mass was extracted from the temperature dependence of the oscillation amplitudes. The amplitude of the dHvA oscillation is damped by the thermal damping factor¹⁶,

$$R_T = \frac{\alpha T m^*}{B \sinh(\alpha T m^*/B)} \quad (2)$$

where the effective mass $m = m^* m_e$. m_e is the bare electron mass, $B = \mu_0 H$ is the magnetic flux density, and $\alpha = 2\pi^2 k_B m_e / \hbar \sim 14.69 \text{ T/K}$. Panel a of Fig. 4 shows dHvA oscillations at temperatures ranging from 300 mK to 25 K. Panel b plots the normalized amplitudes of the peaks and the fitting is of the thermal damping factor from equation (2). For Sample 4, the effective mass increases from $0.16 \pm 0.01 m_e$ to $0.32 \pm 0.01 m_e$ as the angle increases from 15 to 65 degrees. Effective mass anisotropy was seen in very early studies of infrared re-

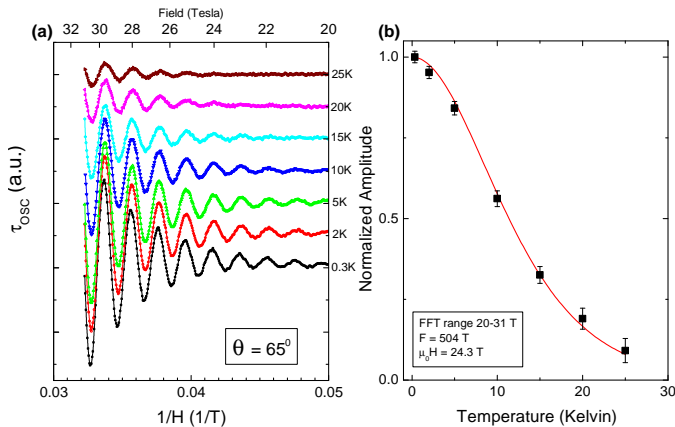


FIG. 4: (color online) Panel a: Temperature dependence of the oscillation amplitude of Sample 4. Panel b: Temperature dependence of the normalized amplitude with fit to the thermal damping factor. Extracted from this fit is a high angle effective mass of $0.32m_e$.

flection on Cu-doped Bi_2Se_3 measuring m_{\parallel}/m_{\perp} to be 4.35.¹⁵

The Fermi velocity, v_F , was determined from the Fermi momentum, k_F^x , and the effective mass by $v_F = \hbar k_F^x/m$. The Fermi velocity is the slope of the energy momentum dispersion. For a quadratic dispersion, v_F increases as k_F^x gets larger. In contrast, for a linear dispersion, it should remain unchanged. In our results for a series of Cu doped Bi_2Se_3 samples, the carrier density varies by an order of magnitude, yet the value of v_F remains approximately constant, as shown in Table II. Samples 3 and 4b are omitted from table II since we only studied their temperature dependence at high angle and thus did not measure their in-plane effective mass.

Compared with undoped Bi_2Se_3 , copper doping increases the Fermi momentum from 0.69 nm^{-1} to 1.00 nm^{-1} ; yet the Fermi velocity remains relatively unchanged. The consistency of the Fermi velocity suggests the possibility of a linear, Dirac-like band in $\text{Cu}_x\text{Bi}_2\text{Se}_3$ as was reported in previous studies.^{12,13}

Further analysis of the quantum oscillation amplitude damping yields the mean free path and scattering time of the samples. Figure 5 shows the Dingle plot of Sample 4, in which the oscillation amplitude is suppressed by the Dingle damping factor, $R_D = \exp[-\alpha T_D m/B]$, where the Dingle temperature $T_D = \hbar/2\pi k_B \tau_S$, $\alpha = 2\pi^2 k_B m_e/e\hbar \sim 14.69 T/K$, and τ_S is the scattering time. This fit gives a Dingle temperature¹⁶ of 57.1 K. From the Dingle temperature, the scattering time τ_S is found to be $2.1 \times 10^{-14} \text{ s}$. The mean free path is also determined from the scattering time and the Fermi velocity by $l = v_F \tau_S$.

The results of the Dingle analysis including the scattering times and mean free paths of the various samples are given in Table III. Samples 3 and 4b are not shown

TABLE II: List of measured Fermi velocities. Last two samples are from our earlier work.¹³ Sample 4b and 3 are not listed here since the temperature dependence for those two samples were taken at high angle.

	$n(10^{19} \text{ cm}^{-3})$	$k_F^x(\text{nm}^{-1})$	$v_F(10^5 \text{ m/s})$
4a	5.93	0.95	6.9
1	6.78	0.94	6.4
2	10.05	0.98	6.0
5	13.91	1.00	6.8
$\text{Cu}_{0.25}\text{Bi}_2\text{Se}_3$	4.3	0.97	5.8
Bi_2Se_3	1.8	0.69	5.7

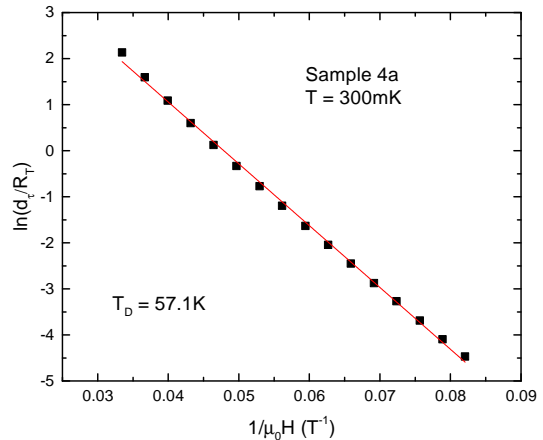


FIG. 5: (color online) Dingle plot of Sample 4a. Fitting is of the Dingle damping factor and it yields a Dingle temperature of 57.1K.

in Table III since we only studied their temperature dependence at high angle and thus could not isolate the Dingle damping from the thermal damping at 0° . Table III also shows the effective mass of the various samples for which temperature dependence was measured at low angle. Sample 4b and 3, for which temperature dependence was measured at high angle, have effective masses of $0.32m_e$ and $0.29m_e$ at 65° and 57° respectively.

With the exception of Sample 4, the scattering times and mean free paths are relatively constant with added carriers varying by 25% in a random fashion. This is consistent with what was reported in the previous dHvA study.¹³ The average scattering time, excluding the outlier, is $5.1 \times 10^{-14} \text{ s}$ and the average mean free path is 31nm. The variance in these parameters is due to sample quality. In the literature for clean samples, the Dingle temperature can be as low as 4 K,¹⁷ and for disordered samples, as high as 9.5 K.¹⁸ This suggests a high level of disorder in our $\text{Cu}_x\text{Bi}_2\text{Se}_3$ samples - especially Sample 4.

Our dHvA effect pattern shows that the electronic

TABLE III: Summary of results from effective mass and Dingle analysis. Last two samples are from our early work.¹³ Sample 4b and 3 are not listed here since the temperature dependence for those two samples were taken at high angle.

	$n(10^{19} \text{cm}^{-3})$	m^*/m_e	$T_D(K)$	$\tau_s(10^{-14} \text{sec})$	$l(\text{nm})$
4a	5.93	0.16	57.1	2.1	15
1	6.78	0.17	20.7	5.9	38
2	10.05	0.19	25.8	4.7	28
5	13.91	0.17	27.7	4.4	30
Cu _{0.25} Bi ₂ Se ₃	4.3	0.19	23.5	5.2	30
Bi ₂ Se ₃	1.8	0.14	23.9	5.1	29

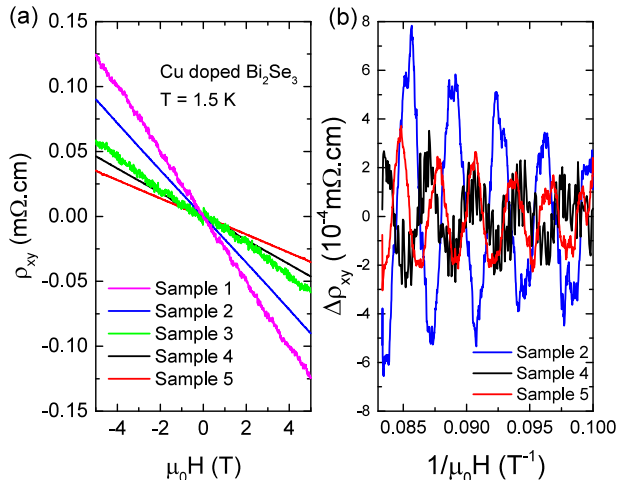


FIG. 6: (color online) Hall effect of the Cu doped Bi₂Se₃. Each sample is cleaved from the same batch as the the samples used in the torque measurement. (Panel a) The Hall signal ρ_{xy} is plotted against field H up to 5 T at $T = 1.5$ K. The Hall signal curves have been antisymmetrized to eliminate the magnetoresistance pickup. The slopes of the $\rho_{xy} - H$ curves are used to determine the Hall carrier density shown in Table IV. (Panel b) Measurements of ρ_{xy} in H up to 12 T show quantum oscillations in three samples. In this panel, a polynomial background is subtracted to show the oscillation signal in ρ_{xy} . The oscillation frequency is found to be the same as the measured frequency in the dHvA effect.

state is single-band. This is supported by the Hall effect measurements. Figure 6(a) shows the Hall effect data of all the Cu-doped Bi₂Se₃ samples taken at $T=1.5$ K. Two keys features are found in the Hall effect data; (a) The Hall signal ρ_{xy} is linear with H , confirming the single-band nature of the electronic state; (b) The carrier density determined by the Hall effect is in close agreement with the carrier density determined from the dHvA effect. Within 12 T at $T=1.5$ K, 3 out of these 5 samples show quantum oscillations in the Hall effect signal (the Shubnikov-de Haas effect, or SdH effect). Table IV shows the Hall carrier density n_H , and the oscillation frequency f_H in the SdH effect. The temperature dependence of the

oscillation frequency is found to be the same as that in the dHvA effect. Moreover, the Hall carrier density is of the same order of magnitude as the carrier density estimated by our Fermi Surface mapping.

TABLE IV: The Hall carrier density n_H with the carrier density determined by the dHvA effect n_M . Quantum oscillation is also observed in a number of samples in the Hall effect measurements up to 12 T. The oscillation frequency F_{0H} and the effective mass m_H in the Hall effect is compared with those of the dHvA effect (labeled as F_{0M} and m_M). For samples that do not reveal quantum oscillations in the Hall effect, we label n/a for m_H and F_{0H} . We measured only one sample from the Sample 4 batch.

	$n_H(10^{19} \text{cm}^{-3})$	$n_M(10^{19} \text{cm}^{-3})$	$F_{0H}(T)$	$F_{0M}(T)$	$\frac{m_H}{m_e}$	$\frac{m_M}{m_e}$
4	6.6	5.93 - 6.31	300	297 - 306	0.15	0.16
1	2.51	6.78	n/a	292	n/a	0.17
3	5.16	7.65	n/a	284	n/a	n/a
2	3.46	10.05	300	317	0.18	0.19
5	8.87	13.91	360	327	0.16	0.17

In addition to determining the electronic state, we also measured the superconducting fraction of Cu doped Bi₂Se₃. The magnetic susceptibility was measured in a Quantum Design Magnetic Property Measurement System 2 weeks after the high field torque experiments. The sample with the lowest carrier concentration shows a superconducting transition with a 16% superconducting volume as seen in Fig. 7. Two of the higher carrier concentration samples showed no superconducting transition. We would like to point out that the superconducting fraction, as well as the superconducting transition temperatures, are quite sensitive to sample aging and the environment - there is even the possibility that they could lose Cu over time and exposure. Therefore, the samples at higher n may or may not have previously been superconducting, but were found not to be when we ran the test for superconductivity.

We note that Sample 4, though having the highest level of disorder, is the only sample to show a superconducting transition. The sample from the previous dHvA study had a Dingle temperature of 23.5 K much like the other samples and it also exhibited superconductivity.¹³ Therefore, it is not the case that superconductivity only occurs in the extreme case of highly disordered samples, rather we suggest that Sample 4 had undergone the least amount of degradation and just happened to be the sample with the highest disorder.

IV. CONCLUSION AND DISCUSSION

Quantum oscillations in magnetization were resolved using highly sensitive torque magnetometry under magnetic fields up to 31 T. A single Fermi pocket was observed to be increasingly elongated as carriers were added

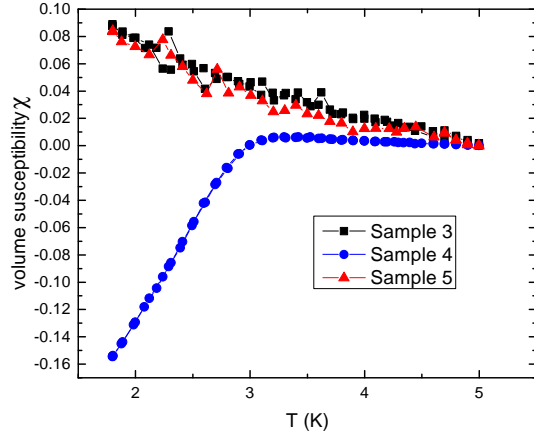


FIG. 7: (color online) Volume susceptibility measurements of 3 different samples. Sample 4, the sample with lowest carrier concentration, shows a superconducting transition at 3 K and a 16% superconducting volume. Samples 3 and 5 do not show any superconducting property most likely due to sample quality degradation over time.

- going from being a closed ellipsoid at low carrier concentration to being quasi-cylindrical at high carrier concentration. Also, we also observed strong anisotropy in the effective mass.

The nature of the transition of the Fermi surface topology is an interesting question. At higher concentration, the elongated 3D ellipsoidal Fermi surface touches the Fermi surface in the neighboring Brillouin Zone, mandating the transition from the 3D Fermi surface to a 2D quasi-cylindrical one. Such a dramatic change of the Fermi surface topology suggests a Lifshitz transition as the Cu brings in extra carriers.

Two experimental consequences are essential to confirm the dimensionality change and probe the nature of the transition. First, at higher n , the quasi-2D Fermi surface should have two quantum oscillation frequencies, a large one from the belly, and a small one from the neck. The large frequency is what we observed in our dHvA measurement¹³ and was confirmed by the SdH measurements.¹¹ In contrast, the small neck frequency was not observed either in our dHvA measurements nor in the SdH results.¹¹ This point is particularly puzzling. We note that these small pockets should exist near the BZ boundary, where the umklapp scattering gets greatly enhanced. The stronger umklapp scattering can greatly reduce the mean free path. Therefore, quantum oscillation measurements at dilution refrigerator temperatures and even higher fields are called for to resolve the second oscillation frequency and to confirm the 3D to 2D transition.

The second consequence of the dimensionality change in the electronic state is the enhancement of thermopower near the 3D to 2D transition. A topology change in the

electronic state usually leads to a large thermopower, a typical signature of the Lifshitz transition.^{19,20} Further thermoelectric measurements are essential to confirm this transition. If the dimensionality changes indeed occur and enhance the thermopower greatly, the Cu doping might lead to another interesting application of topological materials in thermoelectrics.

We further note that close to the dimensionality transition, a strong enough magnetic field may lead to magnetic breakdown. Our current observations do not reveal signature of magnetic breakdown, but future studies with fine tuning of the Cu concentration may reveal the interesting phenomenon of magnetic breakdown.

Acknowledgement We are grateful to discussion with Liang Fu, Kai Sun, and A. Kanigel. The work is supported by the National Science Foundation under Award number ECCS-1307744 (low field torque magnetometry), the Department of Energy under Award number DE-SC0008110 (high field torque magnetometry), by the start up fund and the Mcubed project at the University of Michigan (low field magnetic susceptibility characterization), and by the National Science Foundation under Award number DMR-1255607 (sample growth). The high-field experiments were performed at the National High Magnetic Field Laboratory, which is supported by NSF Cooperative Agreement No. DMR-084173, by the State of Florida, and by the DOE. We thank the assistance of Tim Murphy and Ju-Hyun Park of NHMFL. B. J. Lawson acknowledges the support by the National Science Foundation Graduate Research Fellowship under Grant No. F031543. T. Asaba thanks the support from the Nakajima Foundation.

-
- ¹ L. Fu and C. L. Kane, Phys. Rev. Lett. **100**, 096407 (2008).
 - ² F. Wilczek, Nat. Phys. **5**, 614 (2009).
 - ³ J. E. Moore, Nature (London) **464**, 194 (2010).
 - ⁴ A. Y. Kitaev. Physics-Uspekhi, 44:131 (2001).
 - ⁵ L. Fu and E. Berg, Phys. Rev. Lett. **105**, 097001 (2010).
 - ⁶ Y. S. Hor, A. J. Williams, J. G. Checkelsky, P. Roushan, J. Seo, Q. Xu, H. W. Zandbergen, A. Yazdani, N. P. Ong, and R. J. Cava, Phys. Rev. Lett. **104**, 057001 (2010).
 - ⁷ M. Kriener, K. Segawa, Z. Ren, S. Sasaki, and Y. Ando, Phys. Rev. Lett. **106**, 127004 (2011).
 - ⁸ S. Sasaki, M. Kriener, K. Segawa, K. Yada, Y. Tanaka, M. Sato, and Y. Ando, Phys. Rev. Lett. **107**, 217001 (2011).
 - ⁹ H. Peng, D. De, B. Lv, F. Wei, and C. W. Chu, Phys. Rev. B **88**, 024515 (2013).
 - ¹⁰ N. Levy, T. Zhang, J. Ha, F. Shari, A. A. Talin, Y. Kuk, and J. A. Stroscio, Phys. Rev. Lett. **110**, 117001 (2013).
 - ¹¹ E. Lahoud, E. Maniv, M. S. Petrushevsky, M. Naamneh, A. Ribak, S. Wiedmann, L. Petaccia, Z. Salman, K.B. Chashka, Y. Dagan, and A. Kanigel, Phys. Rev. B **88**, 195107 (2013).
 - ¹² L. A. Wray, S.-Y. Xu, Y. Xia, Y. S. Hor, D. Qian, A. V. Fedorov, H. Lin, A. Bansil, R. J. Cava, and M. Z. Hasan, Nat. Phys. **6**, **855** (2010).
 - ¹³ B. J. Lawson, Y.S. Hor, Lu Li, Phys. Rev. Lett. **109**, 226406 (2012).
 - ¹⁴ H. Kohler and H. Fischer, Phys. Stat. Sol. B **69**, 349 (1975).
 - ¹⁵ L. Tichy and J. Horak, Phys. Rev. B **19**, 1126 (1979).
 - ¹⁶ D. Shoenberg, Magnetic Oscillations in Metals (Cambridge University Press, Cambridge, England, 1984).
 - ¹⁷ J. G. Analytis, J. H. Chu, Y. Chen, F. Corredor, R. D. McDonald, Z.X. Shen, and I.R. Fisher, Phys. Rev. B **81**, 205407 (2010).
 - ¹⁸ K. Eto, Z. Ren, A. A. Taskin, K. Segawa, and Y. Ando, Phys. Rev. B **81**, 195309 (2010).
 - ¹⁹ A. A. Abrikosov, Fundamentals of the theory of metals (North-Holland 1988).
 - ²⁰ V. S. Egorov and A. N. Fedorov, Zh. Eksp. Teor. Fiz. **85**, 1647 (1983).